ACS APPLIED MATERIALS & INTERFACES

Research Article

Cite This: ACS Appl. Mater. Interfaces 2018, 10, 24648−24655

www.acsami.org

Two-Dimensional-Layered Perovskite $ALaTa_2O_7:Bi^{3+}$ (A = K and Na) Phosphors with Versatile Structures and Tunable Photoluminescence

Guojun Zhou,[†] Xingxing Jiang,[‡] Jing Zhao,[†] Maxim Molokeev,[∥,⊥,#] Zheshuai Lin,[‡,§] Quanlin Liu,[†] and Zhiguo Xia*[,†]

[†]The Beijing Municipal Key Laboratory of New Energy Materials and Technologies School of Materials Sciences and Engineering, University of Science and Technology Beijing, Beijing 100083, P. R. China

[‡]Technical Institute of Physics and Chemistry, Chinese Academy of Sciences, Beijing 100190, China

[§]University of Chinese Academy of Sciences, Beijing 100049, China

[∥]Laboratory of Crystal Physics, Kirensky Institute of Physics, Federal Research Center KSC SB RAS, Krasnoyarsk 660036, Russia

[⊥]Siberian Federal University, Krasnoyarsk 660041, Russia

[#]Department of Physics, Far Eastern State Transport University, Khabarovsk 680021, Russia

Supporting Information

ABSTRACT: Topological chemical reaction methods are indispensable for fabricating new materials or optimizing their functional properties, which is particularly important for two-dimensional (2D)-layered compounds with versatile structures. Herein, we demonstrate a low-temperature (~350 °C) ion exchange approach to prefabricate metastable phosphors $ALa_{1-x}Ta_2O_7:xBi^{3+}$ (A = K and Na) with $RbLa_{1-x}Ta_2O_7:xBi^{3+}$ serving as precursors. The as-prepared $ALa_{0.98}Ta_2O_7$:0.02 Bi^{3+} (A = Rb, K, and Na) share the same Dion−Jacobson type 2D-layered perovskite phase, and photoluminescence analyses show that $ALa_{0.98}Ta_2O_7$:0.02 Bi^{3+} (A = Rb, K, and Na) phosphors exhibit broad emission bands peaking at 540, 550, and 510 nm, respectively, which are attributed to the nonradiative transition of Bi^{3+} from excited state $^3P_1$ or $^3P_0$ to ground state $^1S_0$. The various Bi^{3+} local environments at the crystallographic sites enable the different distributions of emission and excitation spectra, and the photoluminescence tuning of $ALa_{0.98}Ta_2O_7$:0.02 Bi^{3+} (A = Rb, K, and Na) phosphors are realized through alkali metal ion exchange. Notably, the combination of superior trivalent bismuth emission and low-temperature ion exchange synthesis leads to a novel yellow-emitting $K(La_{0.98}Bi_{0.02})Ta_2O_7$ phosphor which is successfully applied in a white LED device based on a commercially available 365 nm LED chip. Our realizable cases of this low-temperature ion exchange strategy could promote exploration into metastable phosphors with intriguing properties.

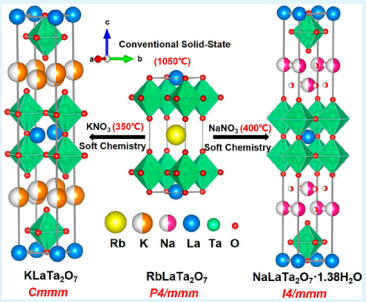

KEYWORDS: *2D-layered perovskite, ion exchange, photoluminescence tuning, Bi^{3+} emission, white light LEDs*

INTRODUCTION

The Dion−Jacobson (DJ) type two-dimensional (2D)-layered perovskite compounds have become a subject of intense research in recent years.[1−4] The DJ type perovskite has the general formula $A[A'_{n-1}B_nO_{3n+1}]$ which consists of negatively charged perovskite-like layers, and a monovalent cation A occupying the interlayer space for compensation of the negative charge, and in the general formula *n* represents the thickness of the perovskite-like layers.[1,5] 2D-layered perovskites with diverse structures have shown promising results for applications such as stable solar cells, photodetectors, light emitting diodes, and so on.[6−8] As is well-known, topological chemical reactions such as ion exchange and intercalation/deintercalation are powerful tools for carrying out structural modifications at low temperatures, and the principle advantage of this method is that the reaction is essentially driven by kinetics.[9−12] Thus, it can be used to obtain metastable phases that are not accessible with traditional high-temperature reactions, and then some new functional materials can be obtained.

Most of the previous research studies in DJ type 2D-laryed perovskites have focused on the investigation of magnetic compounds containing transition metal ions,[10,11,13−16] but these studies rarely paid attention to the luminescent materials.[12] It is expected that the structural modification strategies in layered compounds make it possible to design new metastable phosphors with intriguing properties; in particular, 2D nanosheet luminescence materials could be expected. In present study, we have realized the structural transformation in the DJ type 2D-layered perovskite $ALaTa_2O_7$ (A = alkali metal cations)[17] via low-temperature (~350 °C) melt salt alkali metal ion exchange as illustrated in Scheme 1. During this

Received: May 17, 2018
Accepted: July 3, 2018
Published: July 3, 2018

DOI: 10.1021/acsami.8b08129
ACS Appl. Mater. Interfaces 2018, 10, 24648−24655

Scheme 1. Illustration of the Ion Exchange Process of 2D-Layered Perovskite $ALaTa_2O_7$ (A = Rb, K, and Na)

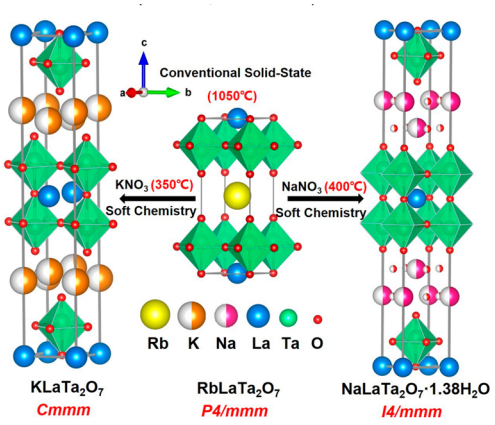

process, $RbLaTa_2O_7$ was first prepared by the conventional solid-state method as the precursor, and then $ALaTa_2O_7$ (A = K and Na) compounds were synthesized by the topological chemical reaction methods, which will be discussed below. Furthermore, the luminescence properties of the designed compounds were investigated upon doping Bi^{3+} as an activator.

As is known to all, luminescent materials with continuously tunable excitation and emission have been intensely studied in recent years due to their wide range of potential applications in areas such as color display technology,[18] solid-state lighting,[19,20] biological sensing,[21] etc.[22] It is well-known that bismuth is another optically active luminescence species[23,24] other than rare earth and other transition metal species, such as Eu^{2+}, Ce^{3+}, Mn^{2+}, Mn^{4+}, and so on.[25−30] Meanwhile, it stands out primarily due to the multiplicity of redox states which can be stabilized in inorganic host materials. In addition, as the heaviest element in the stable main group, bismuth itself has a strong orbital coupling effect, resulting in potential optical performance in a variety of host materials. In particular, trivalent bismuth cations can provide a complex electronic structure that interacts strongly with the corresponding coordination environments, resulting in tunable PL emission.[24,31] Obviously, it is suggested that trivalent bismuth ion could be used as an activator for the application of solid-state lighting.[32,33]

In view of the pertinent band gap values of $ALaTa_2O_7$ (A = alkali metal cations),[34] this could point a way to luminescence emission upon Bi^{3+} doping, and the band structures among them have also been comparatively investigated. $ALa_{1-x}Ta_2O_7{:}xBi^{3+}$ (A = Rb, K, and Na) phosphors with versatile structures and tunable photoluminescence were explored systematically. Experiments show that low-temperature interchanges of alkali metal ions make various local environments of Bi^{3+} activator which affect the movement of emission and excitation spectra, thereby regulating the spectra. Finally, a novel yellow-emitting phosphor $KLa_{1-x}Ta_2O_7{:}xBi^{3+}$ was obtained and implemented successfully in fabrication of a white light emitting diode (WLED) device with a commercially available 365 nm LED chip. This topological chemical reaction method could be highly desired to adjust the local structural environments of activators, which in turn led to interesting light-emitting properties.

EXPERIMENTAL SECTION

Materials and Preparation. $RbLaTa_2O_7$ (abbreviated as RLTO) was prepared by the calcination of a mixture of Rb_2CO_3 (A.R., Aladdin), La_2O_3 (99.99%, Aladdin), and Ta_2O_5 (A.R., Aladdin) (Rb: La: Ta = 1.4:1:2) in air at 1050 °C for 12 h, in which Rb_2CO_3 was present at 1.4 times the stoichiometric value to compensate for the volatilization of rubidium during the high-temperature synthesis. The doping concentration of Bi^{3+} was chosen to be 0.02 mol replacing La^{3+} in $RbLaTa_2O_7$. Samples of $NaLaTa_2O_7$ (abbreviated as NLTO) and $KLaTa_2O_7$ (abbreviated as KLTO) were prepared by ion exchange of $RbLaTa_2O_7$ with the appropriate molten salts through a soft chemical method. The $RbLaTa_2O_7$ powder (0.5 mmol) was heated in molten $NaNO_3$ (10 mmol) or KNO_3 (10 mmol) at 400 or 350 °C, respectively, for 24 h.[17,35]

Characterization. The powder X-ray diffraction (PXRD) measurements were performed on a D8 Advance diffractometer (Bruker Corporation, Germany), operating at 40 kV and 40 mA with Cu Kα radiation (λ = 1.5406 Å). The scanning rate for phase identification was fixed at 8° min^{-1} with a 2θ range from 5° to 60°, and the data for the Rietveld analysis were collected in a step-scanning mode with a step size of 0.02° and 5 s counting time per step over a 2θ range from 5° to 120°. Rietveld refinements were performed by using TOPAS 4.2 software. The energy-dispersive X-ray spectroscopy (EDS) and mapping measurements of the samples were determined at room temperature by scanning electron microscope (SEM, JEOL JSM-6510).

The photoluminescence (PL) and photoluminescence excitation (PLE) spectra were carried out by a fluorescence spectrophotometer (F-4600, HITACHI) equipped with a photomultiplier tube operating at 400 V with a 150 W xenon lamp as the excitation source. The luminescence decay curves were measured by using an FLSP9200 fluorescence spectrophotometer (Edinburgh Instruments Ltd.). The diffuse reflectance spectra were measured on a UV−vis−NIR spectrophotometer (SolidSpec-3700 Shimadzu) with $BaSO_4$ serving as the reference standard.

For the WLED lamp fabrication, the near-UV LED chip (λ = 365 nm) was combined with a yellow-emitting $K(La_{0.98}Bi_{0.02})Ta_2O_7$ phosphor. Optical properties, including the electroluminescence spectrum, color temperature (CCT), color rendering index (Ra), and CIE color coordinates of the LED, were characterized by using a PMS-80 Plus UV−vis−NIR spectrophotocolorimeter (PMS-80, Everfine).

Computational Methods. The band structure and density of state (DOS) of the host materials $ALaTa_2O_7$ (A = Rb, K and Na) are obtained on the basis of first-principles calculations. The first-principles calculations are performed using CASTEP,[36] a plane-wave pseudopotential total energy package based on density functional theory (DFT). Optimized norm-conserving pseudopotentials[37] in Kleinman−Bylander[38] form are employed to model the electron−ion interactions in $ALaTa_2O_7$ (A = Rb, K, and Na) and allow for the use of a relatively small plane-wave basis set without compromising the accuracy required by this study. The Perdew−Burke−Ernzerh of functionals[39] in generalized gradient approximation (GGA) form[40] is adopted to describe the exchange and correlation energy. A high kinetic energy cutoff of 800 eV and dense Monkhorst−Pack k-point meshes spanning less than 0.04 $Å^{-1}$ in the Brillouin zones are chosen. Tests have shown that these computational parameters gave results that are sufficiently accurate for the present purposes.

RESULTS AND DISCUSSION

Synthesis, Structural Evolution, and Characterization. The changing structural features of DJ type 2D-layered perovskite $ALa_{1-x}Ta_2O_7{:}xBi^{3+}$ (A = Rb, K and Na) make it possible to achieve structural transformation. Bi^{3+} is a good activator for fluorescence emission, and in these structures Bi^{3+} can present at various local coordination environments which plays a crucial role in photoluminescence tuning.

DOI: 10.1021/acsami.8b08129
ACS Appl. Mater. Interfaces 2018, 10, 24648−24655

$RbLaTa_2O_7$ can be easily synthesized via high-temperature solid-state reactions, whereas $ALaTa_2O_7$ (A = K and Na) are metastable phases which cannot be obtained by direct high-temperature synthesis. Thus, $NaLaTa_2O_7{\cdot}1.38H_2O$ and $KLaTa_2O_7$ were prepared by topological chemical reactions via melt salt cation exchange with $RbLaTa_2O_7$ precursor and with $NaNO_3$ and KNO_3 serving as the source of corresponding alkali metals (see Scheme 1). Note that the products need to be washed thoroughly with deionized water to remove the excess nitrates. As shown in Figures 1 and 2d–f, all the peaks

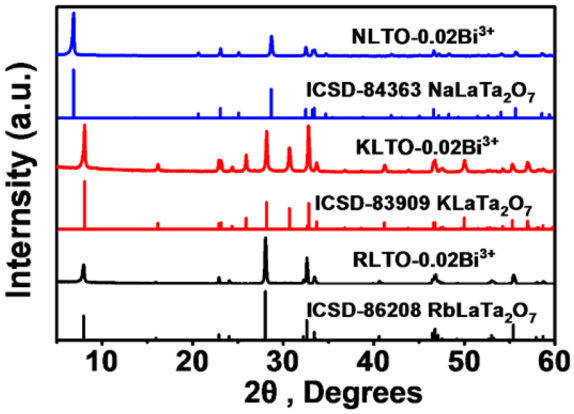

Figure 1. PXRD patterns of $ALa_{0.98}Ta_2O_7$:0.02 Bi^{3+} (A = Rb, K, and Na) samples, together with the standard ICSD cards of the corresponding compounds.

in the PXRD pattern of $ALa_{1-x}Ta_2O_7$:xBi^{3+} (A = Rb, K, and Na) can be successfully indexed on the basis of the ICSD database of the corresponding undoped samples, indicating the formation of single phases. In addition, the EDS technique was used to determine the atomic compositions in $ALaTa_2O_7$ (A = Rb, K, and Na) samples, as shown in Figure S1. The elemental mapping images show that, in these three compounds, Na, K, Rb, La, Ta, and O are homogeneously distributed within each sample. This further demonstrated that the cation exchanges were successful.

Here, the structures of $Na(La_{0.98}Bi_{0.02})Ta_2O_7{\cdot}1.38H_2O$, $K(La_{0.98}Bi_{0.02})Ta_2O_7$, and $Rb(La_{0.98}Bi_{0.02})Ta_2O_7$ are refined by the Rietveld method, and they were crystallized in tetragonal cell, orthorhombic cell, and tetragonal cell structures, respectively. The space group, unit cell parameters, and structure refinement details of these compounds are given in Table 1. Crystal structures of $ALaTa_2O_7$ (A = Rb, K, and Na) were taken as a starting model for Rietveld refinements. Sites of La^{3+} ions in all structures were occupied by La^{3+} and Bi^{3+} ions with fixed occupations of p = 0.98 and p = 0.02, respectively. The occupation of the O^{2-} ion which is associated with the water molecule in $NaLaTa_2O_7{\cdot}1.38H_2O$:0.02 Bi^{3+} was refined, and with the amount of crystallized water refined to be 1.38(6).[41] All refinements were stable and gave low R-factors (Figure 2d–f and Table 1). The atom coordinates and representative bond lengths of $Na(La_{0.98}Bi_{0.02})Ta_2O_7{\cdot}1.38H_2O$, $K(La_{0.98}Bi_{0.02})Ta_2O_7$, and $Rb(La_{0.98}Bi_{0.02})Ta_2O_7$ are given, respectively, in Tables S1 and S2. As shown in Figure 2a–c, all the crystal structures of $ALaTa_2O_7$ (A = Rb, K, and Na) can be described as the same 2D-layered perovskite compounds where the framework layer is built up based on two TaO_6 octahedra with corner sharing. The stacking of adjacent perovskite sheets depends on the ionic radius of cations in the interlayer, and the coordination numbers of Rb, K, and Na cationic functional groups are 8, 6, and 4 in the targeting host materials, respectively.

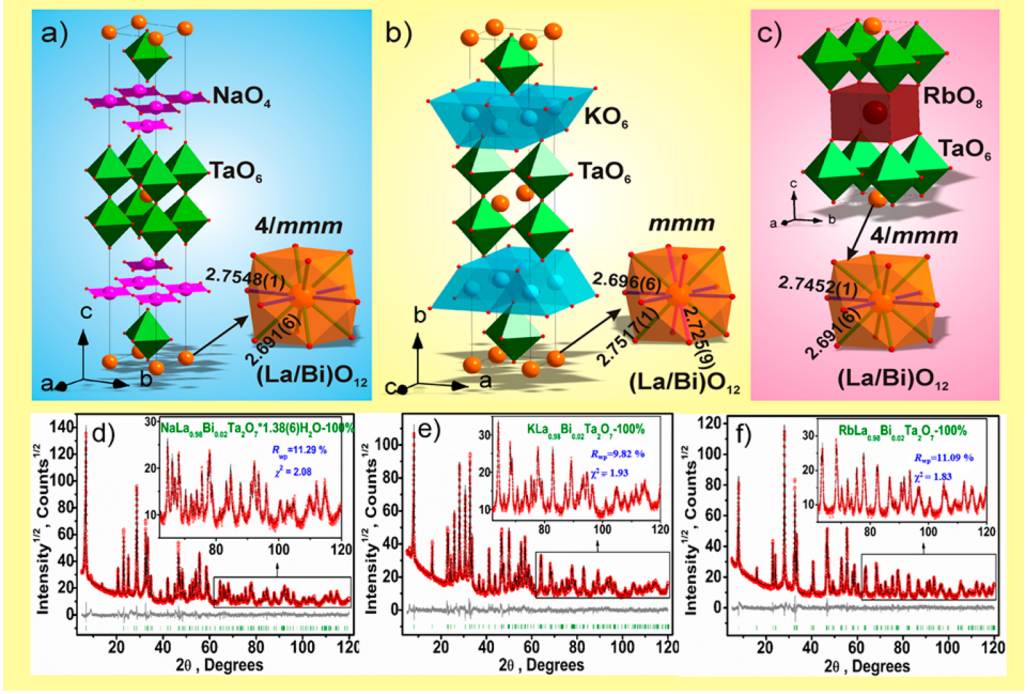

Figure 2. (a–c) Crystal structures of $ALaTa_2O_7$:0.02 Bi^{3+} (A = Rb, K, and Na) highlighting the La/BiO_{12} polyhedra in these layered perovskite compounds. Profile fitting refinement of the selected samples (d) $NaLaTa_2O_7{\cdot}1.38H_2O$:0.02 Bi^{3+}, (e) $KLaTa_2O_7$:0.02 Bi^{3+}, and (f) $RbLaTa_2O_7$:0.02 Bi^{3+}. Observed (red line) and calculated (black line) PXRD patterns. Green vertical lines indicate positions of the Bragg reflections of targeting samples. Gray line represents the difference plot (observed − calculated) on the same scale.

DOI: 10.1021/acsami.8b08129
ACS Appl. Mater. Interfaces 2018, 10, 24648–24655

Table 1. Main Structural Parameters of Processing and Refinement of the Selected Samples

	$NaLaTa_2O_7{\cdot}1.38H_2O{:}0.02Bi^{3+}$	$KLaTa_2O_7{:}0.02Bi^{3+}$	$RbLaTa_2O_7{:}0.02Bi^{3+}$
space group	*I*4/*mmm*	*Cmmm*	*P*4/*mmm*
a, Å	3.89584 (9)	3.89926 (8)	3.88234 (6)
b, Å	3.89584 (9)	21.9005 (6)	3.88234 (6)
c, Å	25.8120 (8)	3.88377 (8)	11.1026 (2)
V, Å^3	391.76 (2)	331.66 (1)	167.345 (6)
Z	2	2	1
2θ interval, deg	5−120	5−120	5−120
R_{wp}, %	11.29	9.82	11.09
R_p, %	8.54	7.44	8.21
R_{exp}, %	5.43	5.09	6.07
χ^2	2.08	1.93	1.83
R_B, %	3.05	2.92	1.72

Identification of Bismuth Concentration and Valence in Doped Samples. In order to determine the effect of Bi^{3+} doping concentration on the formation of targeting phases, we synthesized $RbLa_{1-x}Ta_2O_7{:}xBi^{3+}$ precursors with x = 1%, 2%, 5%, and 10%. The PXRD data of the obtained samples are shown in Figure 3a, and these demonstrate that when the doping concentration of Bi^{3+} ion is higher than 2% impurity peaks were detected. According to the structural refinement results, Bi^{3+} prefers to occupy the La^{3+} site which has a 12-coordination environment. However, as we know, the coordination number of Bi^{3+} ion is typically 5, 6, and 8. Therefore, the doping concentrations of Bi^{3+} are limited due to the different coordination environments between Bi^{3+} and La^{3+} cations.

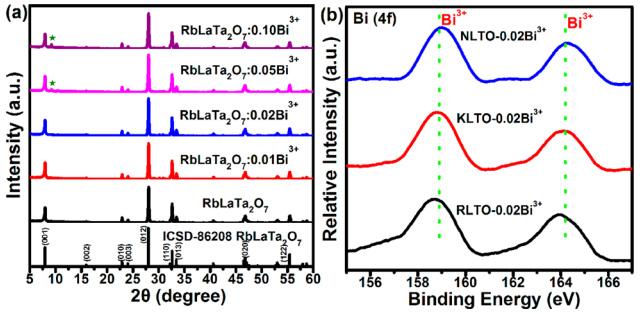

Figure 3. (a) PXRD patterns of the precursor $RbLaTa_2O_7$ with different Bi^{3+} doping concentration (★ represents impurity) and (b) XPS spectra of $A(La_{0.98}Bi_{0.02})Ta_2O_7$ (A = Rb, K, and Na) samples.

In addition, bismuth cations could readily transform into different valence states in solid compounds.[42,43] Meanwhile, the luminescent properties of bismuth are greatly affected by its valence state. Therefore, it is highly essential to identify the valence of bismuth. The X-ray photoelectron spectroscopy (XPS) spectra of $Rb(La_{0.98}Bi_{0.02})Ta_2O_7$, $K(La_{0.98}Bi_{0.02})Ta_2O_7$, and $Na(La_{0.98}Bi_{0.02})Ta_2O_7$ are shown in Figure 3b, which shows two characteristic peaks of Bi^{3+} around 159 and 164 eV due to $4f_{7/2}$ and $4f_{5/2}$, respectively. These results are basically identical to the standard α-Bi_2O_3 spectrum reported in the literature,[44,45] implying the dominance of Bi^{3+} in $ALaTa_2O_7$ (A = Rb, K, and Na) samples.

Luminescence Property Investigation. On the basis of the analysis of crystal structure and bismuth valence state, we systematically studied the optical properties of $A(La_{0.98}Bi_{0.02})$-Ta_2O_7 (A = Rb, K, and Na) phosphors. As can be seen from the normalized excitation and emission spectra in Figure 4a,b, the $Rb(La_{0.98}Bi_{0.02})Ta_2O_7$, $K(La_{0.98}Bi_{0.02})Ta_2O_7$, and $Na(La_{0.98}Bi_{0.02})Ta_2O_7{\cdot}1.38H_2O$ phosphors achieve broad emission bands peaking at 540, 550, and 510 nm when the exciting wavelengths are 310, 325, and 300 nm, respectively. We conjectured that it may be attributed to the nonradiative transition of Bi^{3+} from the excited state $^3P_1$ or $^3P_0$ to the ground state $^1S_0$. Of course, the peculiar luminescence

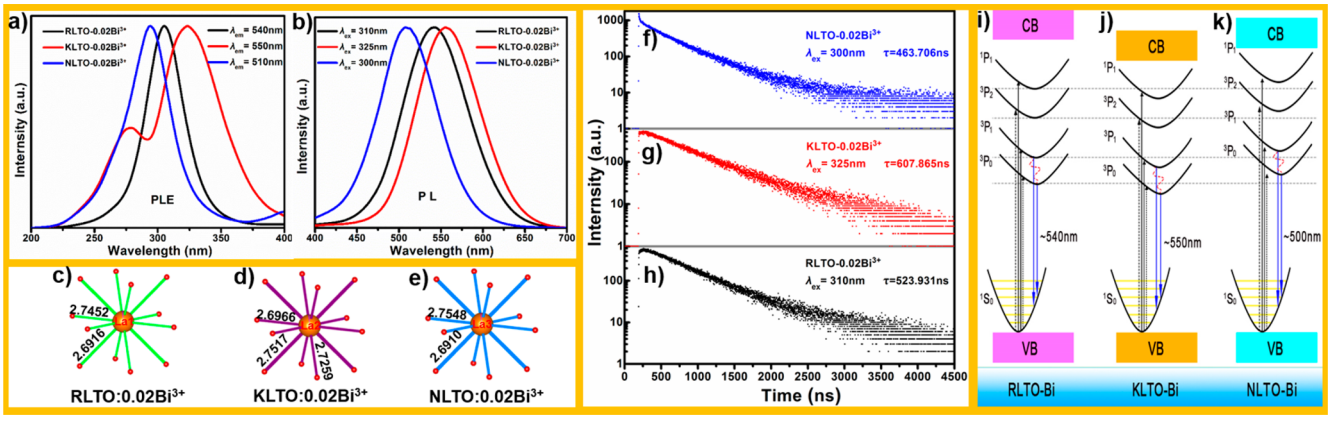

Figure 4. (a, b) Normalized excitation spectra and emission spectra of $A(La_{0.98}Bi_{0.02})Ta_2O_7$ (A = Rb, K, and Na) samples. (c−e) Sites of La^{3+} ions in all host materials are occupied by La^{3+} and Bi^{3+} ions. The coordination environment of activator Bi^{3+} is presented through the bond length of La−O. (f−h) The decay curves upon optimal monitored wavelengths and lifetime values of Bi^{3+} in $A(La_{0.98}Bi_{0.02})Ta_2O_7$ with different alkali metal ion (A), where A = Rb, K, and Na. (i−k) Schematic diagram of luminescence process in $A(La_{0.98}Bi_{0.02})Ta_2O_7$ (A = Rb, K, and Na) phosphors.

DOI: 10.1021/acsami.8b08129
ACS Appl. Mater. Interfaces 2018, 10, 24648−24655

mechanisms for Bi^{3+} have also been outlined on the basis of the experimental results in the previous works.[24,31] The excited phosphors $A(La_{0.98}Bi_{0.02})Ta_2O_7$ (A = Rb, K, and Na) exhibit a symmetric broad emission band in the present work, implying that the Bi^{3+} activator has only one type of local environment in each sample.

It is generally known that the luminescent origin of the Bi^{3+} activator is very complicated and its unique optical properties are easily affected by the crystal structure of the host material. Here, sites of La^{3+} ions in all samples are occupied by La^{3+} and Bi^{3+} ions with fixed occupations of p = 0.98 and p = 0.02, respectively. As shown in Figure 4c–e, the La/Bi–O bond lengths of $A(La_{0.98}Bi_{0.02})Ta_2O_7$ (A = Rb, K, and Na) phosphors are different from each other, indicating the different Bi^{3+} local environments. It should be pointed out that the reduction of the distance between atoms also means the increase of bond covalence. In other words, the crystal field strength could be calculated with the following equation:[46]

$$D_q = \frac{ze^2r^4}{6R^5} \quad (1)$$

Here, the following definitions apply: D_q is the measured crystal field strength, R is the distance between the central ion and its ligands, z is the charge or valence of the anion, e is the charge of an electron, and r is the radius of the d wave function. With this knowledge, it is reasonable to use the average La/Bi–O bond lengths to evaluate the local environment surrounding Bi^{3+} ions. According to the refinement results, the average La/Bi–O bond lengths of $A(La_{0.98}Bi_{0.02})Ta_2O_7$ (A = Rb, K, and Na) are 2.709, 2.724, and 2.712 Å, respectively. This is caused by the difference of the ionic radii of Rb^+, K^+, and Na^+, which lead to different coordination geometries and indirectly cause the distortion of $[La–O_{12}]$ polyhedra, and therefore the average La/Bi–O bond lengths are affected. Since the ion radius of K^+ is smaller than that of Rb^+, a stronger crystal field can be realized from the $Rb(La_{0.98}Bi_{0.02})Ta_2O_7$ to the $K(La_{0.98}Bi_{0.02})Ta_2O_7$ phosphor. As a consequence, we infer that the excited state $^3P_1$ or $^3P_0$ of $K(La_{0.98}Bi_{0.02})Ta_2O_7$ is lower than that of $Rb(La_{0.98}Bi_{0.02})Ta_2O_7$ and leads to the red shift of emission and excitation edges. Obviously, the spectral characteristics could meet this rule, and the red shift of the spectral peak is observed with the reduction of ion radius. Nevertheless, the spectral characteristic of $Na(La_{0.98}Bi_{0.02})Ta_2O_7{\cdot}1.38H_2O$ is inconsistent with the above rule; we suspect that the water molecule entering into the interlayer led to the change in the crystal field environment of Bi^{3+}.

In addition, the decay behavior of the activator in host materials can act as a useful tool to check the origin of fluorescence and give clues to site occupancy information. Figure 4f–h presents the room temperature decay curves of $A(La_{0.98}Bi_{0.02})Ta_2O_7$ (A = Rb, K, and Na) phosphors. The corresponding luminescent decay curves could be fitted using a biexponential temporal dependence according to eq 2:[47]

$$I = A_1 \exp\left(-\frac{t}{\tau_1}\right) + A_2 \exp\left(-t\frac{t}{\tau_2}\right) \quad (2)$$

Here, the following abbrevations apply: I is the luminescence intensity, t is the time after excitation, τ_1 (i = 1, 2) represents the decay time of i component, and parameters A_1 and A_2 are the fitting constants. Using these parameters, the average decay time t can be calculated by the following formula:

$$t = (A_1\tau_1^2 + A_2\tau_2^2)/(A_1\tau_1 + A_2\tau_2) \quad (3)$$

On these bases, the lifetime values of Bi^{3+} ions in $A(La_{0.98}Bi_{0.02})Ta_2O_7$ (A = Rb, K, and Na) phosphors are calculated to be 523.931, 607.865, and 463.706 ns, respectively. There is an obvious difference in the lifetime values for the compositions suggesting the possible phase transition range. Furthermore, it is well-known that the ground state of the trivalent bismuth ion is $^1S_0$ and the excited states in an increasing energy order can be split into the $^3P_0$, $^3P_1$, $^3P_2$, and $^1P_1$ levels. The transitions $^1S_0 \rightarrow {}^3P_0$ or $^3P_2$ are known to be spin-forbidden, whereas $^1S_0 \rightarrow {}^3P_1$ or $^1P_1$ are parity-allowed due to spin–orbit coupling. Therefore, we suppose that the double-exponential decay is caused by the two transitions of $^3P_1 \rightarrow {}^1S_0$ and $^3P_0 \rightarrow {}^1S_0$ that correspond to the short-decay and long-decay components, respectively. This is similar to the previously reported explanation.[23,24]

It is generally known that the band gap of the host material is also a vital factor affecting the luminescence of the Bi^{3+} cation. In order to accurately evaluate the performance of the band gap of hosts, we investigate the band structures and density of state (DOS) based on the first-principles calculations. As shown in Figure 5a–c, the calculated band gaps of $ALaTa_2O_7$ (A = Rb, K, and Na) samples are 4.54, 3.42, and 3.57 eV, respectively.

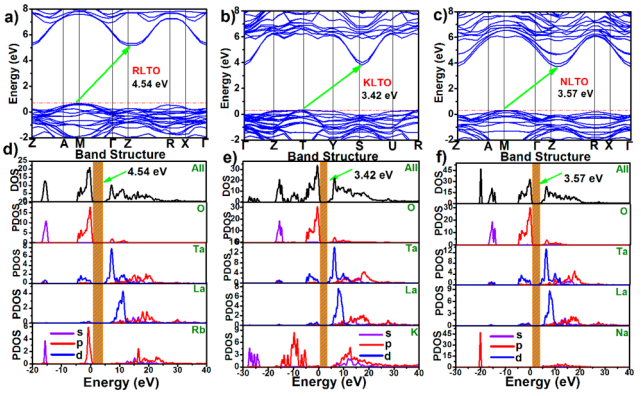

Figure 5. (a–c) Electronic band structures. (d–f) Partial density of state of host groups $A(La_{0.98}Bi_{0.02})Ta_2O_7$ (A = Rb, K, and Na). Forbidden bands are shown in brown regions.

The slight deviation between the calculated and measured band gaps is mainly attributed to the discontinuity of exchange-correlation terms in PBE functionals. It is observed that all the three compounds are typical indirect-transition semiconductors with large k-space between valence band (VB) maximum and conduction band (CB) minimum (Figure 5a–c). This would effectively eliminate the absorption on the stimulating light of the host and guarantee the high PL efficiency. Moreover, the electronic states around the forbidden bands mostly originated from the tantalum and oxygen atoms. In comparison, lanthanum atoms contribute almost nothing to these states, implying that the electronic orbitals within the LaO_{12} polyhedra are rather localized. Thus, the Bi^{3+} ions doped at the lanthanum site would also have a low possibility to generate free carriers under radiation, which would also be favorable for the luminescent application. Therefore, $ALaTa_2O_7$ is a suitable host for luminescent materials doped by Bi^{3+} activator.

DOI: 10.1021/acsami.8b08129
ACS Appl. Mater. Interfaces 2018, 10, 24648–24655

As presented in Figure 6, the optical band gaps of $A(La_{0.98}Bi_{0.02})Ta_2O_7$ (A = Rb, K, and Na) phosphors are

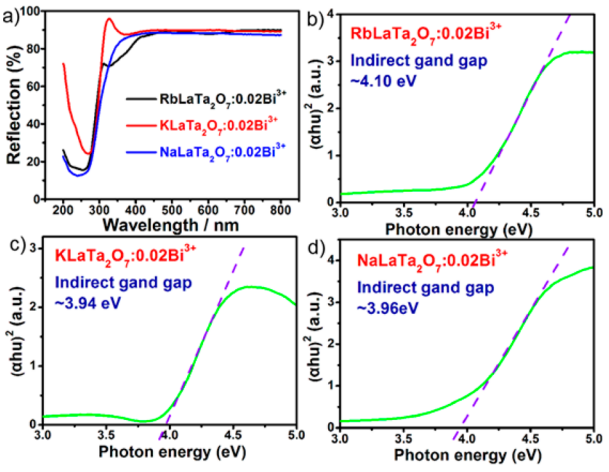

Figure 6. (a) Diffuse reflectance spectra of $A(La_{0.98}Bi_{0.02})Ta_2O_7$ (A = Rb, K, and Na) phosphors and the extrapolations of band gap energy of $A(La_{0.98}Bi_{0.02})Ta_2O_7$ phosphors: (b) A = Rb, (c) A = K, and (d) A = Na.

measured by the diffuse reflection spectra and estimated to be about 4.10, 3.94, and 3.96 eV, respectively. After comprehensive analysis, the schematic illustration of luminescence in $A(La_{0.98}Bi_{0.02})Ta_2O_7$ (A = Rb, K, and Na) phosphors could be summarized on the basis of the comprehensive analysis of spectra and band gaps, as shown in Figure 4i–k. To put it briefly, Bi^{3+} local environments in various crystallographic sites enable the different distributions of emission and excitation spectra owing to the ion exchange of alkaline earth metals, thereby affecting the regulation of the spectrum.

In the process of phosphor applications, thermal stability is one of the most important indicators of phosphor quality. Therefore, it is necessary to conduct a comprehensive study of the thermal quenching of phosphors. The temperature-dependent photoluminescence spectra of $A(La_{0.98}Bi_{0.02})Ta_2O_7$ (A = Rb, K, and Na) phosphors were tested under appropriate excitation at a temperature range room temperature (RT) to 200 °C and with a temperature interval of 25 °C. The detailed experimental results are presented in Figures 7a–c and 8a–d,

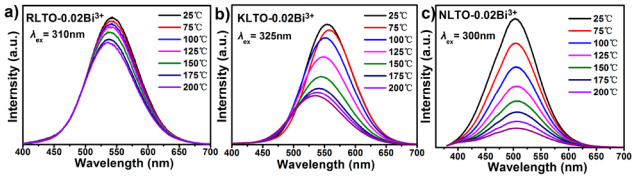

Figure 7. Temperature dependence of emission spectra for 2% Bi^{3+}-doped $ALaTa_2O_7$ phosphors: (a) A = Rb, (b) A = K, and (c) A = Na.

showing that the integrated intensity of emission spectra decreases with increasing temperature. Specifically, the normalized integrated PL intensity of $Rb(La_{0.98}Bi_{0.02})Ta_2O_7$ decreases slightly with increasing temperature, suggesting that the $Rb(La_{0.98}Bi_{0.02})Ta_2O_7$ phosphor has good thermal stability. Nevertheless, the excitation spectrum of the $Rb(La_{0.98}Bi_{0.02})$-Ta_2O_7 phosphor at 250–350 nm is not suitable for WLED applications due to the lack of commercial near-ultraviolet or blue chips. Clearly, the thermal stability of the $Na(La_{0.98}Bi_{0.02})$-

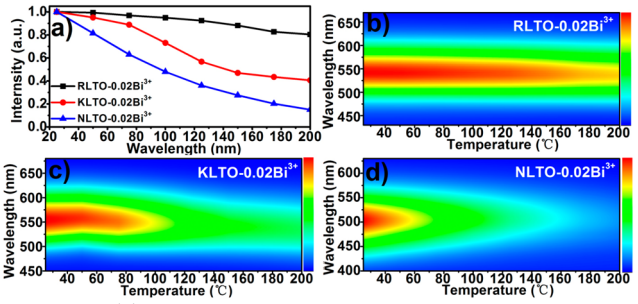

Figure 8. (a) Normalized emission intensity as a function of temperature of $A(La_{0.98}Bi_{0.02})Ta_2O_7$ (A = Rb, K, and Na) phosphors. Temperature-dependent spectral emissions from room temperature to 200 °C for (b) $Rb(La_{0.98}Bi_{0.02})Ta_2O_7$, (c) $K(La_{0.98}Bi_{0.02})Ta_2O_7$, and (d) $Na(La_{0.98}Bi_{0.02})Ta_2O_7$.

$Ta_2O_7 \cdot 1.38H_2O$ phosphor is poor, with a sharp drop in the emission spectral intensity with increasing temperature. Additionally, the normalized integrated PL intensity of the $K(La_{0.98}Bi_{0.02})Ta_2O_7$ phosphor decreases with increasing temperature from 25 to 200 °C, and with about 50% emission intensity remaining at 150 °C. Taking into account the spectral characteristics and thermal stability properties of these three phosphors, $K(La_{0.98}Bi_{0.02})Ta_2O_7$ is the yellow-emitting phosphor with the hightest potential for use in UV chip based WLED applications. Considering the practical application of the $K(La_{0.98}Bi_{0.02})Ta_2O_7$ phosphor, we recorded the internal quantum efficiencies (IQEs), which is another important parameter to consider for practical application. It can be calculated using the following expression:[48]

$$\eta_{IQE} = \frac{\int L_S}{\int E_R - \int E_S} \quad (4)$$

Here, L_S is the emission spectrum. E_S is the spectrum of the light used to excite the sample, and E_R is the spectrum of the excitation light without the sample in the integrating sphere. The IQE of a typical $K(La_{0.98}Bi_{0.02})Ta_2O_7$ phosphor was measured upon 325 nm excitation, and the corresponding value is 42.3%.

CIE Chromaticity Coordinates and EL Spectrum of WLED Lamp. The corresponding CIE chromaticity diagram calculated from the emission spectra of $A(La_{0.98}Bi_{0.02})Ta_2O_7$ (A = Rb, K, and Na) samples and their corresponding digital images upon 254 nm UV lamp excitation are shown in Figure 9a. The yellow-emitting $KLaTa_2O_7$:0.02 Bi^{3+} phosphor with the CIE color coordinate of (0.3860, 0.5618) was chosen to be

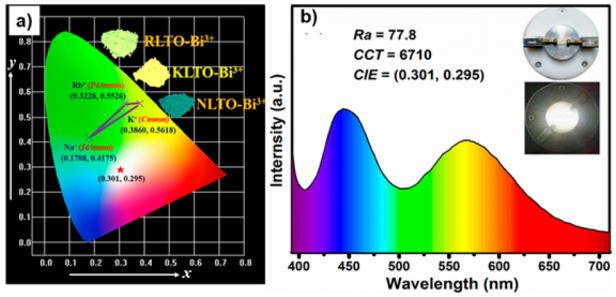

Figure 9. (a) CIE coordinates and digital photos of $A(La_{0.98}Bi_{0.02})$-Ta_2O_7 (A = Rb, K, and Na) phosphors. (b) Electroluminescent spectrum of the fabricated WLED.

DOI: 10.1021/acsami.8b08129
ACS Appl. Mater. Interfaces 2018, 10, 24648–24655

applied in UV chip pumped WLED. On this basis, we combined blue-emitting $BaMgAl_{10}O_{17}:Eu^{2+}$ and yellow-emitting $K(La_{0.98}Bi_{0.02})Ta_2O_7$ with a commercial UV LED chip (λ = ~365 nm) to realize white light emission. The electroluminescence (EL) spectrum of the white LED lamp is shown in Figure 9b. It revealed a CIE color coordinate of (0.301, 0.295) with the white light correlated color temperature (CCT) of 6710 K and the color rendering index (Ra) of 77.8, indicating that $K(La_{0.98}Bi_{0.02})Ta_2O_7$ is a good candidate for an UV-excitable white-emitting phosphor.

CONCLUSION

In summary, three kinds of DJ type 2D-layered perovskites were comparatively investigated, and novel metastable $K(La_{0.98}Bi_{0.02})Ta_2O_7$ and $Na(La_{0.98}Bi_{0.02})Ta_2O_7{\cdot}1.38H_2O$ were obtained by topological low-temperature (~350 °C) ion exchange with $Rb(La_{0.98}Bi_{0.02})Ta_2O_7$ serving as precursor. The fluorescence spectra study show that $A(La_{0.98}Bi_{0.02})Ta_2O_7$ (A = Rb, K, and Na) phosphors exhibit broad emission bands peaking at 540, 550, and 510 nm, respectively, which are attributed to the nonradiative transition of Bi^{3+} from excited state $^3P_1$ or $^3P_0$ to ground state $^1S_0$. The interactions between alkali metals and La/Bi−O_{12} make a variety of local environments for Bi^{3+} activator which affect the movement of emission and excitation spectra, thereby realizing the regulation of the spectra. In view of the above facts, a yellow-emitting $K(La_{0.98}Bi_{0.02})Ta_2O_7$ phosphor has been implemented successfully in the fabrication of WLED device with a commercially available 365 nm LED chip. This strategy of low-temperature ion exchange opens up new opportunities to delve into new types of phosphors with metastable phases.

ASSOCIATED CONTENT

Supporting Information

The Supporting Information is available free of charge on the ACS Publications website at DOI: 10.1021/acsami.8b08129.

Element mapping images and EDS composition analysis of some mentioned samples, and fractional atomic coordinates, isotropic displacement parameters, and main bond lengths (Å) of some mentioned compounds (PDF)

Crystal structure of $K(La_{0.98}Bi_{0.02})Ta_2O_7$ (CIF)

Crystal structure of $Na(La_{0.98}Bi_{0.02})Ta_2O_7{\cdot}1.38H_2O$ (CIF)

Crystal structure of $Rb(La_{0.98}Bi_{0.02})Ta_2O_7$ (CIF)

AUTHOR INFORMATION

Corresponding Author

*E-mail: xiazg@ustb.edu.cn.

ORCID

Xingxing Jiang: 0000-0001-6068-8773

Jing Zhao: 0000-0002-8000-5973

Zheshuai Lin: 0000-0002-9829-9893

Quanlin Liu: 0000-0003-3533-7140

Zhiguo Xia: 0000-0002-9670-3223

Notes

The authors declare no competing financial interest.

ACKNOWLEDGMENTS

The authors acknowledge the support from the National Natural Science Foundation of China (Nos. 51722202, 91622125, and 51572023) and the Natural Science Foundations of Beijing (2172036) and RFBR (17-52-53031).

REFERENCES

(1) Strayer, M. E.; Gupta, A. S.; Akamatsu, H.; Lei, S.; Benedek, N. A.; Gopalan, V.; Mallouk, T. E. Emergent Noncentrosymmetry and Piezoelectricity Driven by Oxygen Octahedral Rotations in n = 2 Dion−Jacobson Phase Layer Perovskites. *Adv. Funct. Mater.* **2016**, *26*, 1930−1937.

(2) Mao, L.; Ke, W.; Pedesseau, L.; Wu, Y.; Katan, C.; Even, J.; Wasielewski, M. R.; Stoumpos, C. C.; Kanatzidis, M. G. Hybrid Dion-Jacobson 2D Lead Iodide Perovskites. *J. Am. Chem. Soc.* **2018**, *140*, 3775−3783.

(3) Ziegler, C.; Dennenwaldt, T.; Weber, D.; Duppel, V.; Kamella, C.; Podjaski, F.; Tuffy, B.; Moudrakovski, I.; Scheu, C.; Lotsch, B. V. Functional Engineering of Perovskite Nanosheets: Impact of Lead Substitution on Exfoliation in the Solid Solution $RbCa_{2-x}Pb_xNb_3O_{10}$. *Z. Anorg. Allg. Chem.* **2017**, *643*, 1668−1680.

(4) Ida, S.; Ogata, C.; Eguchi, M.; Youngblood, W. J.; Mallouk, T. E.; Matsumoto, Y. Photoluminescence of Perovskite Nanosheets Prepared by Exfoliation of Layered Oxides, $K_2Ln_2Ti_3O_{10}$, $KLnNb_2O_7$, and $RbLnTa_2O_7$ (Ln: Lanthanide Ion). *J. Am. Chem. Soc.* **2008**, *130*, 7052−7059.

(5) Porob, D. G.; Maggard, P. A. A Rapid Flux-Assisted Synthetic Approach Towards the Bandgap Engineering of Layered Perovskites. *Chem. Mater.* **2007**, *19*, 970−972.

(6) Cao, D. H.; Stoumpos, C. C.; Farha, O. K.; Hupp, J. T.; Kanatzidis, M. G. 2D Homologous Perovskites as Light-Absorbing Materials for Solar Cell Applications. *J. Am. Chem. Soc.* **2015**, *137*, 7843−7850.

(7) Nazarenko, O.; Kotyrba, M. R.; Yakunin, S.; Aebli, M.; Raino, G.; Benin, B. M.; Worle, M.; Kovalenko, M. V. Guanidinium-Formamidinium Lead Iodide: A Layered Perovskite-Related Compound with Red Luminescence at Room Temperature. *J. Am. Chem. Soc.* **2018**, *140*, 3850−3853.

(8) Kim, H. G.; Tran, T. T.; Choi, W.; You, T.-S.; Halasyamani, P. S.; Ok, K. M. Two New Non-centrosymmetric n = 3 Layered Dion−Jacobson Perovskites: Polar $RbBi_2Ti_2NbO_{10}$ and Nonpolar $CsBi_2Ti_2TaO_{10}$. *Chem. Mater.* **2016**, *28*, 2424−2432.

(9) Kodenkandath, T. A.; Kumbhar, A. S.; Zhou, W. L.; Wiley, J. B. Construction of Copper Halide Networks within Layered Perovskites. Syntheses and Characterization of New Low-Temperature Copper Oxyhalides. *Inorg. Chem.* **2001**, *40*, 710−714.

(10) De Laune, B.; Rees, G.; Marco, J.; Hah, H.; Johnson, C.; Johnson, J.; Berry, F.; Hanna, J.; Greaves, C. Topotactic Fluorine Insertion into the Channels of $FeSb_2O_4$-Related Materials. *Inorg. Chem.* **2017**, *56*, 10078−10089.

(11) Ishikawa, H.; Yajima, T.; Miyake, A.; Tokunaga, M.; Matsuo, A.; Kindo, K.; Hiroi, Z. Topochemical Crystal Transformation from a Distorted to a Nearly Perfect Kagome Cuprate. *Chem. Mater.* **2017**, *29*, 6719−6725.

(12) Liu, B. M.; Zhang, Z. G.; Zhang, K.; Kuroiwa, Y.; Moriyoshi, C.; Yu, H. M.; Li, C.; Zheng, L. R.; Li, L. N.; Yang, G.; Zhou, Y.; Fang, Y. Z.; Hou, J. S.; Matsushita, Y.; Sun, H. T. Unconventional Luminescent Centers in Metastable Phases Created by Topochemical Reduction Reactions. *Angew. Chem., Int. Ed.* **2016**, *55*, 4967−4971.

(13) Hayward, M. A.; Green, M. A.; Rosseinsky, M. J.; Sloan, J. Sodium Hydride as a Powerful Reducing Agent for Topotactic Oxide Deintercalation: Synthesis and Characterization of the Nickel(I) Oxide $LaNiO_2$. *J. Am. Chem. Soc.* **1999**, *121*, 8843−8854.

(14) Taylor, D. D.; Schreiber, N. J.; Brown, C. M.; Arevalo-Lopez, A. M.; Rodriguez, E. E. Stabilization of cubic Sr_2FeMoO_6 through topochemical reduction. *Chem. Commun.* **2015**, *51*, 12201−12204.

(15) Pratt, J. A.; Shepherd, A. M.; Hayward, M. A. Diamagnetic Ru^{2+} in $Na_2La_2Ti_2RuO_{10-x}$ ($0 < x < 2$): A Series of Complex Oxides Prepared by Topochemical Reduction. *Inorg. Chem.* **2015**, *54*, 10993−10997.

(16) Mikita, R.; Aharen, T.; Yamamoto, T.; Takeiri, F.; Ya, T.; Yoshimune, W.; Fujita, K.; Yoshida, S.; Tanaka, K.; Batuk, D.;

DOI: 10.1021/acsami.8b08129
ACS Appl. Mater. Interfaces 2018, 10, 24648−24655

Abakumov, A. M.; Brown, C. M.; Kobayashi, Y.; Kageyama, H. Topochemical Nitridation with Anion Vacancy-Assisted N^{3-}/O^{2-} Exchange. *J. Am. Chem. Soc.* **2016**, *138*, 3211−3217.
(17) Suzuki, H.; Tomita, O.; Higashi, M.; Abe, R. Design of Nitrogen-doped Layered Tantalates for Non-sacrificial and Selective Hydrogen Evolution from Water under Visible Light. *J. Mater. Chem. A* **2016**, *4*, 14444−14452.
(18) Tang, Z.; Wang, D.; Khan, W. U.; Du, S.; Wang, X.; Wang, Y. Novel Zirconium Silicate Phosphor $K_2ZrSi_2O_7:Eu^{2+}$ for White Light-emitting Diodes and Field Emission Displays. *J. Mater. Chem. C* **2016**, *4*, 5307−5313.
(19) Xia, Z.; Liu, Q. Progress in Discovery and Structural Design of Color Conversion Phosphors for LEDs. *Prog. Mater. Sci.* **2016**, *84*, 59−117.
(20) Xia, Z.; Meijerink, A. Ce^{3+}-Doped Garnet Phosphors: Composition Modification, Luminescence Properties and Applications. *Chem. Soc. Rev.* **2017**, *46*, 275−299.
(21) Zhang, F.; Wong, S. S. Ambient Large-scale Template-mediated Synthesis of High-aspect Ratio Single-crystalline, Chemically Doped Rare-earth Phosphate Nanowires for Bioimaging. *ACS Nano* **2010**, *4*, 99−112.
(22) Gai, S.; Li, C.; Yang, P.; Lin, J. Recent Progress in Rare Earth Micro/nanocrystals: Soft Chemical Synthesis, Luminescent Properties, and Biomedical Applications. *Chem. Rev.* **2014**, *114*, 2343−2389.
(23) Kang, F.; Zhang, Y.; Peng, M. Controlling the Energy Transfer via Multi Luminescent Centers to Achieve White Light/tunable Emissions in a Single-phased X2-type $Y_2SiO_5:Eu^{3+},Bi^{3+}$ Phosphor for Ultraviolet Converted LEDs. *Inorg. Chem.* **2015**, *54*, 1462−1473.
(24) Kang, F.; Zhang, H.; Wondraczek, L.; Yang, X.; Zhang, Y.; Lei, D. Y.; Peng, M. Band-Gap Modulation in Single Bi^{3+}-Doped Yttrium−Scandium−Niobium Vanadates for Color Tuning over the Whole Visible Spectrum. *Chem. Mater.* **2016**, *28*, 2692−2703.
(25) Chen, M.; Xia, Z.; Molokeev, M. S.; Wang, T.; Liu, Q. Tuning of Photoluminescence and Local Structures of Substituted Cations in $xSr_2Ca(PO_4)_2-(1-x)Ca_{10}Li(PO_4)_7:Eu^{2+}$ Phosphors. *Chem. Mater.* **2017**, *29*, 1430−1438.
(26) Chen, M.; Xia, Z.; Molokeev, M. S.; Lin, C. C.; Su, C.; Chuang, Y.-C.; Liu, Q. Probing Eu^{2+} Luminescence from Different Crystallographic Sites in $Ca_{10}M(PO_4)_7:Eu^{2+}$ (M = Li, Na, and K) with β-$Ca_3(PO_4)_2$-Type Structure. *Chem. Mater.* **2017**, *29*, 7563−7570.
(27) Jin, Y.; Fang, M. H.; Grinberg, M.; Mahlik, S.; Lesniewski, T.; Brik, M. G.; Luo, G. Y.; Lin, J. G.; Liu, R. S. Narrow Red Emission Band Fluoride Phosphor $KNaSiF_6:Mn^{4+}$ for Warm White Light-Emitting Diodes. *ACS Appl. Mater. Interfaces* **2016**, *8*, 11194−11203.
(28) Lin, C. C.; Meijerink, A.; Liu, R. S. Critical Red Components for Next-Generation White LEDs. *J. Phys. Chem. Lett.* **2016**, *7*, 495−503.
(29) Lee, S. P.; Liu, S. D.; Chan, T. S.; Chen, T. M. Synthesis and Luminescence Properties of Novel Ce^{3+}- and Eu^{2+}- Doped Lanthanum Bromothiosilicate $La_3Br(SiS_4)_2$ Phosphors for White LEDs. *ACS Appl. Mater. Interfaces* **2016**, *8*, 9218−9223.
(30) Zhu, Q.-Q.; Wang, L.; Hirosaki, N.; Hao, L. Y.; Xu, X.; Xie, R.-J. Extra-Broad Band Orange-Emitting Ce^{3+}-Doped $Y_3Si_5N_9O$ Phosphor for Solid-State Lighting: Electronic, Crystal Structures and Luminescence Properties. *Chem. Mater.* **2016**, *28*, 4829−4839.
(31) Kang, F.; Peng, M.; Lei, D. Y.; Zhang, Q. Recoverable and Unrecoverable Bi^{3+}-Related Photoemissions Induced by Thermal Expansion and Contraction in $LuVO_4:Bi^{3+}$ and $ScVO_4:Bi^{3+}$ Compounds. *Chem. Mater.* **2016**, *28*, 7807−7815.
(32) Cao, R.; Quan, G.; Shi, Z.; Gou, Q.; Chen, T.; Hu, Z.; Luo, Z. Synthesis and Luminescence Properties of $LiBaPO_4:Bi^{3+}$ Yellow-emitting Phosphor for Solid-state Lighting. *J. Mater. Sci.: Mater. Electron.* **2018**, *29*, 5287−5292.
(33) Cao, R.; Quan, G.; Shi, Z.; Luo, Z.; Hu, Q.; Guo, S. A Double Perovskite $Ca_2MgWO_6:Bi^{3+}$ Yellow-emitting Phosphor: Synthesis and Luminescence Properties. *J. Lumin.* **2017**, *181*, 332−336.
(34) Machida, M.; Yabunaka, J.-i.; Kijima, T. Synthesis and Photocatalytic Property of Layered Perovskite Tantalates, $RbLnTa_2O_7$ (Ln = La, Pr, Nd, and Sm). *Chem. Mater.* **2000**, *12*, 812−817.
(35) Toda, K.; Honma, T.; Ye, Z.-G.; Sato, M. Synthesis and Structure Determination of New Layered Perovskite Compound, $KLaTa_2O_7$. *J. Alloys Compd.* **1997**, *249*, 256−259.
(36) Clark, S. J.; Segall, M. D.; Pickard, C. J.; Hasnip, P. J.; Probert, M. I. J.; Refson, K.; Payne, M. C. First Principles Methods Using CASTEP. *Z. Kristallogr. - Cryst. Mater.* **2005**, *220*, 567−570.
(37) Rappe, A. M.; Rabe, K. M.; Kaxiras, E.; Joannopoulos, J. D. Optimized Pseudopotentials. *Phys. Rev. B: Condens. Matter Mater. Phys.* **1990**, *41*, 1227−1230.
(38) Kleinman, L.; Bylander, D. M. Efficacious Form for Model Pseudopotentials. *Phys. Rev. Lett.* **1982**, *48*, 1425−1428.
(39) Perdew, J. P.; Burke, K.; Ernzerhof, M. Generalized Gradient Approximation Made Simple. *Phys. Rev. Lett.* **1996**, *77*, 3865−3868.
(40) Perdew, J. P.; Chevary, J. A.; Vosko, S. H.; Jackson, K. A.; Pederson, M. R.; Singh, D. J.; Fiolhais, C. Atoms, Molecules, Solids, and Surfaces: Applications of the Generalized Gradient Approximation for Exchange and Correlation. *Phys. Rev. B: Condens. Matter Mater. Phys.* **1992**, *46*, 6671−6687.
(41) Toda, K.; Uematsu, K.; Sato, M. Structure Determination of New Layered Perovskite Compound, $NaLaTa_2O_7$, Synthesized by Ion-exchange Reaction. *Nippon Seramikkusu Kyokai Gakujutsu Ronbunshi* **1997**, *105*, 482−485.
(42) Cao, R.; Peng, M.; Wondraczek, L.; Qiu, J. Superbroad Near-to-mid-infrared Luminescence from Bi_5^{3+} in $Bi_5(AlCl_4)_3$. *Opt. Express* **2012**, *20*, 2562−2571.
(43) Kang, F.; Peng, M. A New Study on the Energy Transfer in the Color-tunable Phosphor $CaWO_4$:Bi. *Dalton. Trans.* **2014**, *43*, 277−284.
(44) Kang, F.; Peng, M.; Zhang, Q.; Qiu, J. Abnormal Anti-quenching and Controllable Multi-transitions of Bi^{3+} Luminescence by Temperature in a Yellow-emitting $LuVO_4:Bi^{3+}$ Phosphor for UV-converted White LEDs. *Chem. - Eur. J.* **2014**, *20*, 11522−11530.
(45) Kang, F.; Zhang, Y.; Wondraczek, L.; Zhu, J.; Yang, X.; Peng, M. Processing-dependence and the Nature of the Blue-shift of Bi^{3+}-related Photoemission in $ScVO_4$ at Elevated Temperatures. *J. Mater. Chem. C* **2014**, *2*, 9850−9857.
(46) Duan, C.; Reid, M. A Simple Model for f→d Transitions of Rare-earth Ions in Crystals. *J. Solid State Chem.* **2003**, *171*, 299−303.
(47) Huang, C.-H.; Chen, T.-M.; Liu, W.-R.; Chiu, Y.-C.; Yeh, Y.-T.; Jang, S.-M. A Single-Phased Emission-Tunable Phosphor $Ca_9Y(PO_4)_7:Eu^{2+},Mn^{2+}$ with Efficient Energy Transfer for White-Light-Emitting Diodes. *ACS Appl. Mater. Interfaces* **2010**, *2*, 259−264.
(48) Miao, S.; Xia, Z.; Zhang, J.; Liu, Q. Increased Eu^{2+} Content and Codoping Mn^{2+} Induced Tunable Full-color Emitting Phosphor $Ba_{1.55}Ca_{0.45}SiO_4:Eu^{2+},Mn^{2+}$. *Inorg. Chem.* **2014**, *53*, 10386−10393.

DOI: 10.1021/acsami.8b08129
ACS Appl. Mater. Interfaces 2018, 10, 24648−24655